Eur Biophys J (1998) 27: 83–98

ARTICLE

Martin Oheim · Dinah Loerke
Walter Stühmer · Robert H. Chow

The last few milliseconds in the life of a secretory granule

Docking, dynamics and fusion visualized by total internal reflection fluorescence microscopy (TIRFM)

Received: 26 June 1997 / Accepted: 26 September 1997

Abstract We have monitored single vesicles (granules) in bovine adrenal chromaffin cells using an optical sectioning technique, total internal reflection fluorescence microscopy (TIRFM). With TIR, fluorescence excitation is limited to an optical slice near a glass/water interface. In cells located at the interface, granules loaded with fluorescent dye can be visualized near to or docked at the plasma membrane. Here we give evidence that (1) TIRFM resolves single vesicles and (2) the fluorescence signal originates from vesicles of roughly 350 nm diameter, presumably large dense core vesicles (LDCVs). (3) Diffusional spread of released vesicle contents can be resolved and serves as a convenient criterion for a fusion event. (4) We give details on vesicle properties in resting cells, such as lateral mobility of chromaffin granules, number density, and frequency of spontaneous fusion or withdrawal into the cytoplasm. (5) Upon stimulation with high extracellular potassium, TIRFM reports depletion of the 'visible pool' of vesicles closest to the plasma membrane within hundreds of milliseconds, consistent with previous concepts of a release-ready pool. We conclude that TIRFM constitutes an independent assay for pool depletion. TIRFM will allow us to study aspects of secretion that have previously been inaccessible in living cells, in particular the spatial relations and dynamics of vesicles prior to and during exocytosis and re-supply of the near-membrane pool of vesicles.

M. Oheim (✉) · D. Loerke · W. Stühmer
Max-Planck-Institute for Experimental Medicine,
Department of Molecular Biology of Neuronal Signals,
Hermann-Rein Strasse 3, D-37075 Göttingen, Germany
(e-mail: oheim@mail.mpiem.gwdg.de)
(e-mail: loerke@mail.mpiem.gwdg.de)
(e-mail: stuhmer@mail.mpiem.gwdg.de)

M. Oheim · R. H. Chow
University of Edinburgh Medical School,
Department of Physiology, Membrane Biology Group,
Teviot Place, EH8 9AG, Scotland, UK
(e-mail: rchow@holyrood.ed.ac.uk)

Key words TIRF · Evanescent wave microscopy · Optical sectioning · Ca^{2+}-triggered exocytosis · Visible pool · Chromaffin cell · Vesicle fusion

Abbreviations *TIR* Total internal reflection · *TIRFM* Total internal reflection fluorescence microscopy · *LDCV* Large dense core vesicle · *h*-Planck's constant $6.6261 \cdot 10^{-34}$ Js · *CCD* Charge coupled device · *AO* Acridine orange · *FI* Fluorescence intensity · *EM* Electron microscopy

1 Introduction

During recent years, molecular biologists have cloned many neuronal proteins that are believed to play roles in orchestrating the vesicle life cycle (Südhof 1995; Südhof and Rizo 1996). Functional studies in neuronal or neurosecretory cells have been challenging because many steps of vesicle maturation occur in the nanometer domain adjacent to the plasma membrane. Furthermore, the final steps of calcium-(Ca^{2+}-) triggered vesicle fusion take place on a time-scale of a few hundred microseconds.

Imaging techniques have proved very powerful in studying highly localized gradients of intracellular free calcium concentrations, $[Ca^{2+}]_i$ (Cheek et al. 1989; Etter et al. 1994), but few of the published imaging approaches can provide the resolution and signal-to-noise ratio required to quantify events in such a demanding spatiotemporal regime as vesicle fusion (Llinas et al. 1992; Smith et al. 1993; Monck et al. 1994). In the absence of adequate optical methods, authors have resorted to mathematical modeling (Chad and Eckert 1984; Neher 1986; Llinas et al. 1992; Chow et al. 1994; Klingauf and Neher 1997), estimating the timecourse and concentration of submembrane $[Ca^{2+}]_i$ that triggers exocytosis.

Confocal microscopy (Pawley 1995) and multiphoton excitation fluorescence microscopy (Denk et al. 1990; Lipp and Niggli 1993; Piston et al. 1994; Denk et al. 1996; Svoboda et al. 1996) resolve subcellular structures at very

high spatial resolution, mainly because of their effective suppression of out-of-focus light (Agard et al. 1989; Hiraoka et al. 1990). However, their time resolution has been limited by the scanning rate.

1.1 Total internal reflection microscopy

Total internal reflection fluorescence microscopy (TIRFM) (see Axelrod et al. (1992) for a recent review) selectively excites dye molecules in an aqueous environment directly adjacent to a glass interface. As applied to biological cell cultures, TIRFM allows selective visualization, for example, of cell/substrate contact regions (Axelrod 1981). By restricting fluorescence excitation to a thin optical layer adjacent to the interface to which cells adhere, TIRF microscopy eliminates out-of-focus fluorescence present in conventional epifluorescence excitation. It thereby permits the observation of molecular processes directly at the plasma membrane, even of single molecular interactions (Funatsu et al. 1995; Macklin et al. 1996). Thus TIRF microscopy can be used to visualize the position, extent and motion of these contact regions (Axelrod 1981; Gingell et al. 1985; Lanni et al. 1985; Olveczky et al. 1997), or to determine dynamics (Huang et al. 1994), concentrations and kinetics (Lassen and Malmsten 1996; Cleeman and Morad 1997) of fluorophores and their reactions as a function of distance from the interface.

Using TIRFM in living cells, we have monitored single labeled vesicles from the time that they approach a ~260-nm thin, subplasmalemmal section and bind to the plasma membrane to the time they undergo exocytosis. We give evidence that TIRFM constitutes an independent assay for secretion and is a powerful tool that can be used to reveal the dynamics of single secretory granules. Part of this work has been published in abstract form (Oheim et al. 1997).

2 Theory

2.1 Fluorescence excitation by TIR

A light beam striking an interface between two media, 1 (e. g. glass) and 2 (e. g. aqueous solution), with refractive indices n_1 and n_2, respectively, is totally reflected if $n_1 > n_2$ and if the angle of incidence θ_i exceeds the critical angle θ_c, defined by $\theta_c = \arcsin(n_2/n_1)$ (Fig. 1 a, b). Owing to interference of the incident and reflected light beam a standing wave is generated in the optically rarer medium. This *'evanescent wave'* decays exponentially with distance z from the interface,

$$E(\Psi, z) = E_0(\Psi)\,\exp(-z/d_p)\,, \qquad (1)$$

where Ψ is the polarization angle of the incident light beam and d_p is called the penetration depth. $E_0(\Psi)$ is the electric field amplitude at the interface, at $z=0$. The penetration depth d_p is defined as the distance over which the electric field amplitude falls off to $1/e$ of its value at the surface, and is a function of beam and setup parameters,

$$d_p = \lambda_0 / \left(2\pi n_1 \sqrt{\sin^2\theta_i - (n_2/n_1)^2}\right), \qquad (2)$$

where λ_0 is the wavelength of the incident light beam in vacuum (~air) (Harrick 1965; 1967). For excitation intensities that do not elicit photobleaching (as discussed below, photobleaching was not a significant problem in our recordings), fluorescence excited by the evanescent wave will therefore be proportional to the exponentially decaying excitation intensity times the fluorophore distribution integrated over the excitation and collection volumes.

3 Materials and methods

3.1 Cell preparation

Bovine adrenal chromaffin cells were enzymatically dispersed and cultured in glass-bottomed chambers for two days in a CO_2 incubator at 37 °C in DMEM + 10% FCS + 2 ml penicillin/streptomycin + 5 ml GMS-X supplement (100×) (all obtained from Gibco, Life Technologies, Paisley, Scotland). Immediately prior to experiments, cells were perfused with external solution (145 mM NaCl, 10 mM HEPES (pH 7.2), 2.8 mM $MgCl_2$, 2 mM $CaCl_2$). High potassium extracellular solution used to trigger exocytosis contained 60 mM KCl, 85 mM NaCl, 10 mM HEPES (pH 7.2), 2.8 mM $MgCl_2$, 2 mM $CaCl_2$. Experiments were performed at room temperature (~20–23 °C). Cellular swelling and subsequent cell lysis were considered as indicators of damage. Therefore, cells were imaged by means of bright field microscopy both before and after exposure to laser light.

3.2 Staining of vesicles

Vesicles were stained using acidotropic dyes, exploiting the low intravesicular pH of ~5.5 (Winkler and Westhead 1980). Cells were incubated either for 3 minutes with 5 µM acridine orange (AO) (λ_{ex}^{max}=501 nm, λ_{em}^{max}=511 nm, Sigma, St. Louis, MO) at 37 °C, or for 30 minutes with 40 nM *Lysotracker* Green (λ_{ex}^{max}=489 nm, $\lambda_{em}^{max}\approx$520 nm, Molecular Probes, Eugene, OR) added to the cell culture medium. Before the recordings, cells were washed 6 times with external solution containing no stain.

Bleaching was found to be negligible at the integration times and photon flux densities used.

3.3 Optical system

3.3.1 Setup geometry and general layout

We used the 'prism approach' (Axelrod 1981) with a hemicylindrical BK-7 prism of 5 mm radius (Spindler & Hoyer,

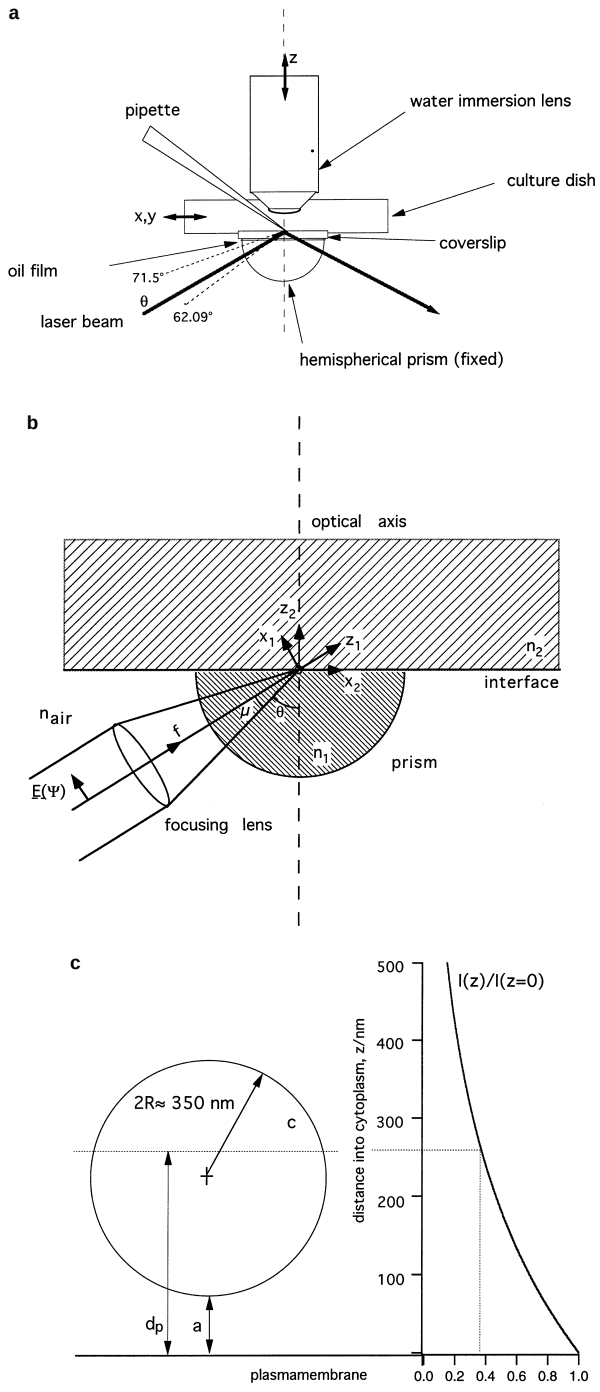

Fig. 1 Setup geometry **a** Schematic of the variable-angle-TIRF microscope. Cells are cultured in glass-bottomed culture-dishes that are coupled to the prism using low fluorescence immersion oil. Prism and objective are fixed and centred to the optical (z_2–) axis, whereas the chamber slides in the x_2–y_2 plane on the oil film. A moveable cantilever allows evanescent fluorescence excitation at multiple angles of incidence. **b** Simplified view used for calculating the evanescent field intensity. This calculation makes use of the approximation that the refractive indices of prism, coupling oil and coverslip are equal, i. e. $n_{prism} \approx n_{oil} \approx n_{coverslip} = n_1$. **c** Idealized geometry near the interface used to calibrate the decay length d_p of the evanescent field, $I(z)/I(z=0) = \exp(-z/d_p)$. Vesicles are assumed spherical and homogeneously dye-filled. R is the vesicular radius, $a = z - R$ is the distance from the interface to the bottom of the vesicle, c is the intravesicular dye concentration

Göttingen, Germany) and an upright microscope (Zeiss Axioskop, Jena, Germany). Objectives were either a Zeiss 100× 1.0w NA or 60× 0.9w NA (Olympus, Hamburg, Germany), lens. Coverslips ($n = 1.52$) were purchased from Menzel (Braunschweig, Germany). Very low fluorescence oil with $n = 1.5180$ was a gift from Leica (Bensheim, Germany).

The components of the setup were arranged so as to allow simple control of the angle of incidence of excitation and to reduce the amount of adjustment required before each experiment (Fig. 1 a). The microscope, prism and laser optics (details below) were moved together as a unit, relative to a fixed stage, on which were located the recording chamber and the micromanipulator used to hold the patch-clamp headstage and pipette. The flat top of the prism was optically coupled to the fixed glass bottom of the recording chamber by a thin oil layer. The center of symmetry for the entire system was the midpoint of the flat top of the hemicylindrical prism, at which the laser beam was aimed at all times, regardless of the angle of incidence (see below).

3.3.2 Fluorescence excitation

A water-cooled argon-ion Laser (L-3500, Lexel Laser, Inc., Fremont, CA, USA), running at 488 nm TEM00 with a beam radius ($1/e^2$ intensity) of 1.0 mm, was coupled into a single-mode fibre via a piezo-driven fiber launcher (Polytec GmbH, Waldbronn, Germany). We monitored the excitation intensity with a photodiode to enable corrections for fluctuations in the laser output, which were $\leq \pm 0.2\%$ in the light control mode. Fibre exit, focusing lens and aperture were mounted on a cantilever swinging around the midpoint of the hemicylindrical prism. Reflection of scattered light was minimized by using high surface quality (80-50SQ, flatness 9 fringes) and coating all surfaces with a black matt finish. The $1/e^2$ beam radius at the fibre output was 900 μm, with a divergence angle of 0.028°. A set of neutral density (ND) filters (Omega, Battleboro, VT, USA) was used to attenuate the laser intensity to ~1 mW pre-fibre, corresponding to $\sim 0{,}65 \times 1$ mW = 0.65 mW post-fibre. The photon flux density (photons $s^{-1}\,\mu m^{-2}$) at the focus was $0.65\ \text{mW} \cdot 0.95/(4.067 \cdot 10^{-19}\ \text{J} \cdot 1.21328 \cdot 10^3\ \mu m^2) = 1.251 \cdot 10^{12}$ photons $s^{-1} \times \mu m^{-2}$. To minimize photodamage to cells, a mechanical shutter (Uniblitz, Optilas, Puchheim, Germany) restricted illumination to the periods of data acquisition.

3.3.3 Angle of incidence and critical angle

The direction of excitation beam propagation and the optical axis (x_1, y_1, z_1) of the optical microbench (Spindler & Hoyer) were colinear, and they were normal to the curved prism surface (Fig. 1 b). The focal point of the beam was at the center (x_2, y_2) = (0, 0) of the flat surface of the coverslip. Before entering the lens, the linearly polarized beam had a polarization direction that had an angle $\Psi = 0$ with

its projection onto the plane of incidence of the central wave. Angle μ defined the exit pupil of the lens, n_{air}, n_1 and n_2 were the refractive indices of air, prism and aqueous solution, respectively.

Incidence angle θ was measured from the normal to the prism's planar surface to the beam's central axis. The calculated critical angle was $(62.06 \pm 1.2)°$, assuming values of $n_2 = 1.33$ to 1.36 for the cell cytoplasm and $n_1 = 1.5224$ (at $\lambda = 488$ nm) for BK-7 glass. Owing to the uncertainty in n_2, we chose to determine θ_c experimentally and calibrate the angular scale with respect to it. We determined θ_c by increasing θ until we observed TIR. We then used an angular precision table (Spindler & Hoyer) to adjust the angle of incidence θ with $5' = 1/12°$ accuracy.

3.3.4 Beam geometry and evanescent excitation

The focused laser beam enters the hemicylindrical prism and hits the interface at an angle θ. The lateral (x, y) evanescent wave intensity profile can be calculated numerically (Burghardt and Thompson 1984). For the setup geometry, the evanescent $1/e^2$ width in (x, y) direction (and thus the area containing 95% of the excitation light) is approximately equivalent to the $1/e^2$ widths in a plane slicing the incident beam at angle θ. The spot size of an unbound focused laser beam is given by $w_2 = F\lambda/(\pi w_1 n_2)$ (Marom et al. 1979), where $w_1 = 900$ µm and w_2 are the beam waists, $f = 110$ mm is the focal length and $n_2 = 1.5224$ is the refractive index of the prism. Substituting yields $w_2 = 12.47$ µm. With $\theta = 66.5°$, the long axis is 12.47 µm/cos (66.5°) = 31.27 µm. The centre of the Gaussian profile is not at $x = 0$ but at $7.5\ \lambda_0/2\pi = 0.58$ µm. This displacement of the beam focus is due to the Goos-Hänchen shift (Goos and Hänchen 1947). The axes of the profile can be varied by changing the incidence angle or the focal length of the lens compared to incident beam's $1/e^2$ radius.

3.3.5 Fluorescence data acquisition

We define a volume given by the $1/e$ axial decay in the z direction (Eqs. (1) and (2), Fig. 1 c) and the lateral (x, y) $1/e^2$ spot size (Fig. 2 a) as the '*evanescent region*'. Accurate focusing was achieved by a piezo-electric device mounted between the objective revolver and the lens (Polytec). Fluorescence emission and residual scattered excitation light were separated by a D488/10× clean-up filter, HQ500LP dichroic and Q500LP emission filter (all from Chroma Technology, Brattleboro, VT, USA).

We sampled fluorescence with a spatial frequency of 75 (at 100×) or 125 nm (at 60×) using a frame-transfer CCD camera (Visitron, Puchheim, Germany). The imaging system was based on a 1-MHz 12-bit air-cooled camera (Micro-Max, Princeton Instruments, Trenton, NJ, USA) with an EEV-37 1024×512 pixel frame-transfer chip having 15-µm pixelsize and 200,000 electrons full-well capacity. Taking into account Rayleigh's definition of resolution and Nyquist's sampling theorem, a total magnification of $2 \times \text{pixelsize} \times \text{NA}/(0.61\lambda)$ will yield a diffraction limited image of a 'resel' on a single $(15\ \mu\text{m})^2$ pixel of the camera chip. This roughly amounts to an additional 0.98- and 1.47-fold magnification for the 1.0 NA 100× and 0.9 NA 60× lenses. We optimised our optical system for the respective lens by changing the tube lens using an Optovar magnifier (Zeiss).

Images were transferred directly to the 96 MB memory of a P55/200 MHz Pentium computer via a high-speed serial link. Images were taken at an acquisition rate of 10 Hz, with an integration time of 60 ms for each image.

3.4 Data analysis

We either defined a subarray of interest and plotted fluorescence intensity (FI) histograms, or scanned consecutive images, looking at FIs of single spots. The latter allows one to trace the movement *and* intensity of fluorescent spots and extract spatial information from TIRF images, whereas the former allows one to trace even minute changes in FI. Analysis was performed on a PPC8200/120 Macintosh computer using the public domain *'NIH image'* program. We fitted Gaussian distributions to the clearly resolvable peaks in FI histograms,

$$f(FI) = K_0 + K_1 \exp(-((FI - K_2)/K_3)^2) \tag{3}$$

where $f(FI)$ is the normalized number of events, i. e. the number of pixels at a given FI divided by the number of pixels within the image of the cell bottom, K_0 is a constant offset, K_1 is proportional to the area of the peak, K_2 is the central displacement along the intensity axis, and K_3 characterizes the width of the bell-shaped Gaussian, i. e. the intensity differences in the image.

3.4.1 Relating changes in fluorescence to single vesicle fluorescence

We derived the fluorescence signal that arises from a single, spherical homogeneously stained vesicle at a distance a from the interface as it is excited by the evanescent field. Let R be the radius and c the dye concentration, then

$$FI(a; d_p, R, c, I_0) \propto \pi \cdot c \cdot I_0 \cdot \int_a^{2R+a} \exp(-z/d_p)\,(Rz - z^2)\,\mathrm{d}z\,, \tag{4}$$

which is a function of the variable a and the parameters d_p and R. To determine the penetration depth of the evanescent field, we took the ratio of $FI_{tir}(a; R, I_{0,tir}, \theta, d_p, x_2, y_2)/FI_{tir}(a = 0, R, I_{0,tir}, \theta, d_p, x_2, y_2)$ at different distances for a given angle of incidence, $\theta = 66.5°$. We integrated the fluorescence over the bead, taking the averaged signal from at least 10 beads for each radius. Taking the fluores-

cence ratio eliminated the proportionality constant in Eq. (4).

$$\frac{FI(a; d_p, R)}{FI(0; d_p, R)} = \frac{\int_a^{2R+a} \exp(-z/d_p)\,(Rz - z^2)\,\mathrm{d}z}{\int_0^{2R} \exp(-z/d_p)\,(Rz - z^2)\,\mathrm{d}z}, \qquad (5)$$

Beads of radii of 0.1, 0.2, 0.5 and 2 μm (Molecular Probes, Eugene, OR, USA) were attached by suction to the tip of a patch pipette and then positioned in the evanescent field with a piezo-manipulator (Fig. 2 b). The distance between bead and glass bottom was measured with ±4 nm precision by focusing at the interface and then at the centre of the bead with the piezoelectric focus control. We averaged signals from at least 10 beads at different levels, integrating the fluorescence over each bead.

4 Results

In this study, TIRF microscopy was used to investigate the spatial and temporal pattern of secretory vesicle dynamics in bovine adrenal chromaffin cells both at rest and after stimulation. Prior to studying cells under TIR illumination (4.2), we characterized the performance of our instrument, using fluorescent beads (4.1).

4.1 In vitro experiments

4.1.1 Calibration of the penetration depth, d_p

Plotting $FI_{tir}(a; R)/FI_{epi}(0; R)$ versus a for bead radii of 0.2 and 0.5 as well as 2 μm yielded an exponentially decaying fluorescence ratio as a was increased. Data points were best described with a $1/e$ space constant, d_p, of (261 ± 2) nm (Fig. 2 d). The lateral extent of the evanescent region was found to be somewhat larger than our calculations, $1/e^2$ axes were 32.0 μm and 80.25 μm. The evanescent penetration depth did not vary appreciably with lateral position (x_2, y_2) (data not shown).

At larger distances from the interface, a second component of excitation light became dominant (see Fig. 2 d, inset); extrapolating this component linearly to $a = 0$, we estimated the fraction of non-evanescent fluorescence at $a = 0$ to be less than 3.8%. Whereas the evanescent component rapidly decayed the propagating light was almost independent of a. Such an observation would be consistent with the presence of higher laser modes. Measurements of the beam intensity profile however confirmed the Gaussian profile expected for TEM00.

4.1.2 Resolution along the optical (z–) axis

In order to focus at a given depth from the interface, we first focused at the interface and then measured the distance to the new plane of focus using the calibrated voltage of the piezoelectric focus drive. Uncertainty in measurements of fluorescence intensity at a fixed plane is introduced by fluctuations in excitation intensity and signal readout noise. We define dz as the distance over which movements of a fluorescent bead would lead to variations in fluorescence intensity equal to that due to fluctuations in excitation intensity and signal readout. To estimate dz, we measured the average fluorescence signal and standard deviation, σ^2, of 100-nm beads held in position at the tip of a patch pipette. Fluorescence of a given bead fluctuated ±1.07%, corresponding to variations in bead location of ±2.81 nm at $d_p = 261$ nm. We define a signal five times above this fluctuation as resolvable. Thus, the z-resolution of our instrument is about ±15 nm.

4.2 Experiments with stained chromaffin cells

4.2.1 Fluorescent spots visualized under evanescent excitation

Chromaffin cells (Fig. 3 a) were incubated with acidotropic dyes. Epi-illumination images appeared blurred and structureless (Fig. 3 b). In contrast, TIR illumination revealed numerous fluorescent spots (Fig. 3 c), which were readily discerned owing to the dramatic reduction in background fluorescence. In resting cells, these spots showed little variation over time apart from a weak lateral agitation.

The following sections describe experiments performed to test the hypothesis that the fluorescent spots are secretory granules. If they are single secretory granules, they should be of the right size; they should disappear upon secretagogue application, perhaps coincident with a small cloud of released fluorescent dye. Furthermore, maintained stimulation should lead to the disappearance of spots, with kinetics appropriate to the exhaustion of the release-ready pool of docked granules; finally, anything that blocks exocytosis should block the disappearance of the spots.

4.2.2 Size of fluorescent spots

A histogram of $1/e^2$ spot diameters taken from 100 spots from different cells was fitted with a Gaussian distribution (Fig. 3 d). The average spot diameter was 350.7 ± 28.2 nm. A second, minor peak was centered at 480 nm (Fig. 3 d, see discussion).

4.2.3 Spot density under non-stimulated conditions and spontaneous events

The number of fluorescent spots per μm^2 (Fig. 3 c) was (1.07 ± 0.11) μm^{-2} (data from 34 cells at rest). Rarely, individual spots were seen to disappear spontaneously.

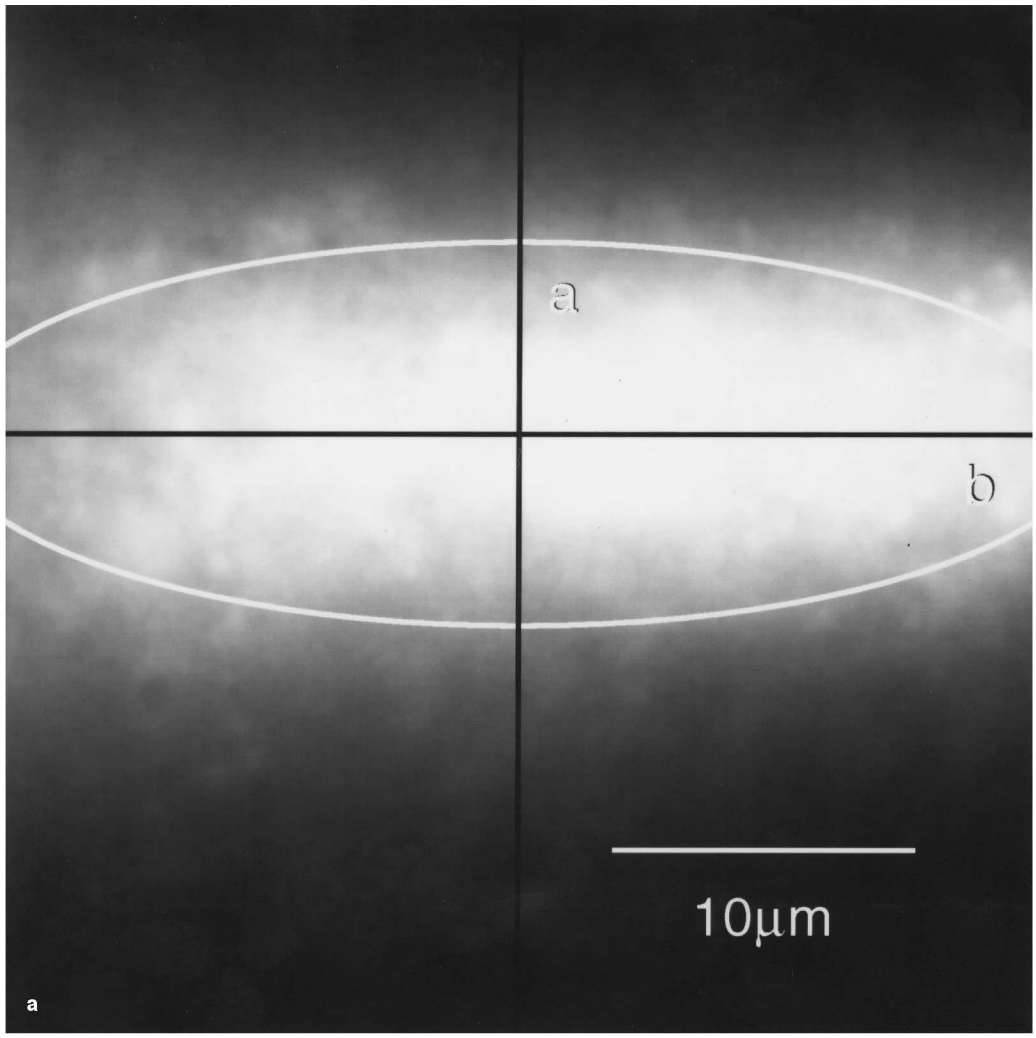
a
b
10µm
a

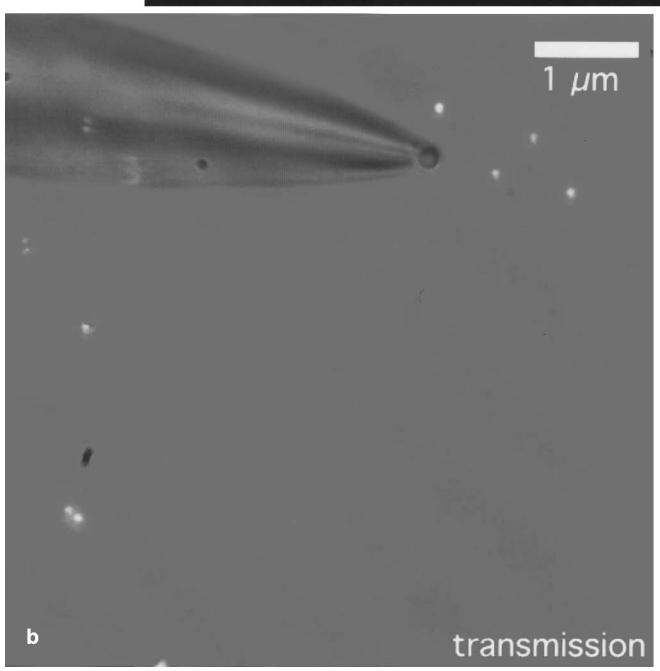
1 µm
b
transmission

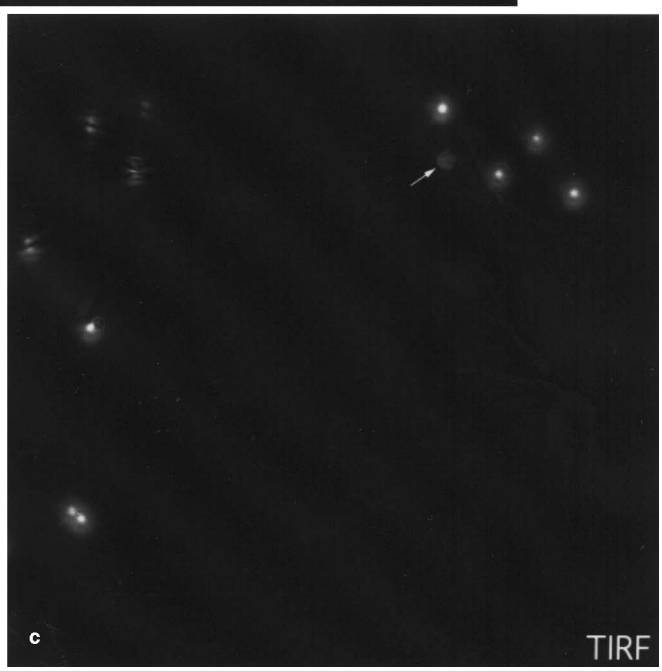
c
TIRF

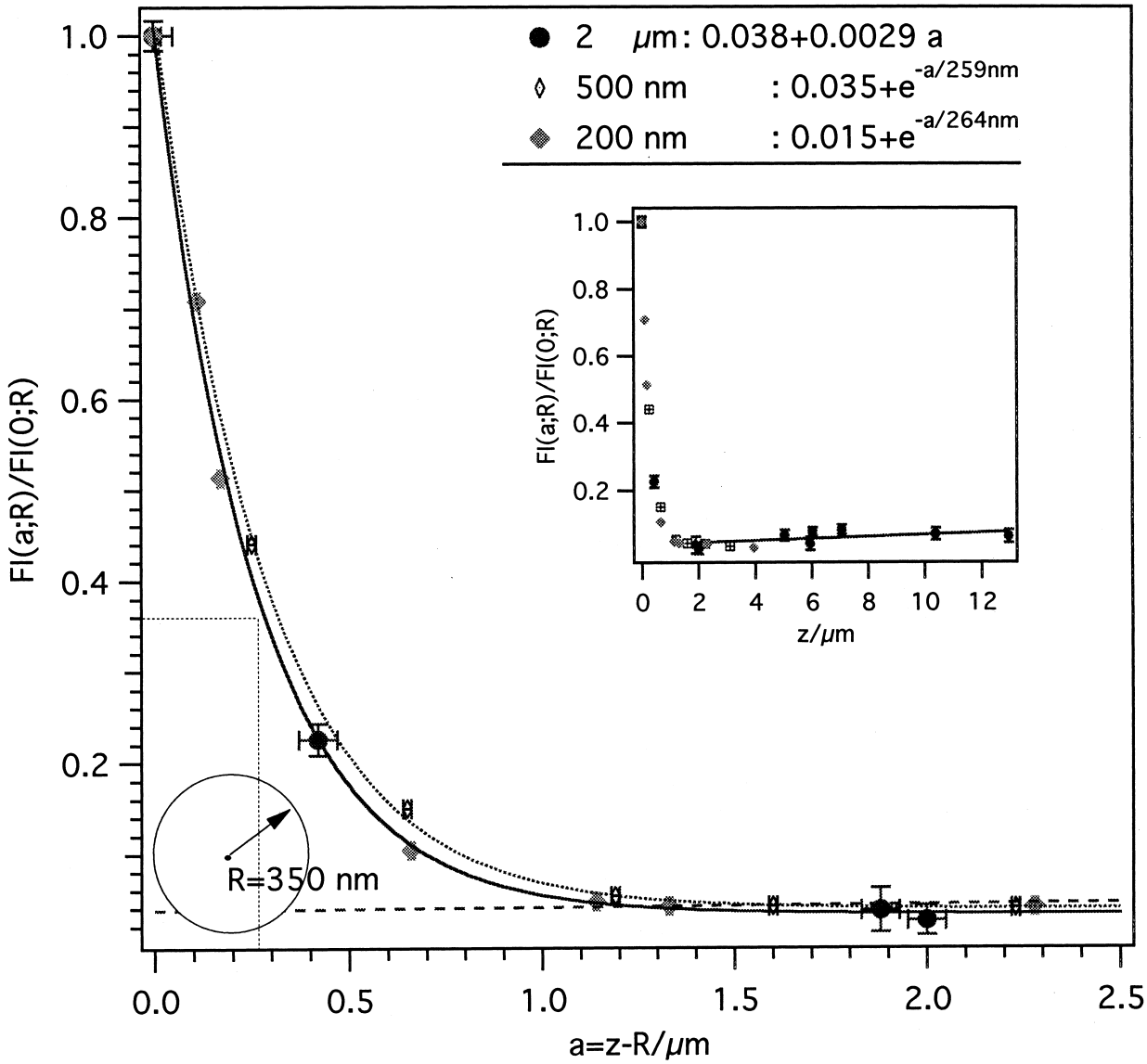

d

Fig. 2 Calibration of the penetration depth. **a** TIRF images of a 20 μM solution of AO, focusing at the interface layer ($z=0$). The elongated Gaussian has $1/e^2$ half axes of 32.0 μm and 80.25 μm, respectively. $1/e^2$ beam diameter at the fibre exit was 900 μm, focused at the midpoint of the hemicylindrical prism with a $f=110$ mm lens. $\theta=66.5°$, $\lambda=488$ nm. **b** Bright-field image of an aqueous suspension of 200 nm latex beads, one of them attached to the tip of a patch pipette, at 190 nm above the surface. The focus is at the tip of the pipette. Bead fluorescence is due to evanescent excitation. The scalebar indicates 1 μm. **c** TIRF image of 200 nm yellow-green fluorescently labelled latex beads directly at the interface and attached to the tip of a patch-pipette. Focus at $a=190$ nm. Fluorescence excitation at $\lambda=488$ nm at an angle of incidence, $\theta=66.5°$, resulted in a space constant d_p of 261 nm. **d** Calibration of the penetration depth of the evanescent wave upon total internal reflection of a polarized Ar^+-ion laser, running at 488 nm TEM00. The beam was incident at $\theta=66.5°$. We plotted the ratio $FI_{tir}(a; R)/FI_{epi}(0; R)$ versus the distance from the interface to the bottom of the bead, a. The graph pools data from 200, 500 nm, and 2 μm beads (see legend). The space constant, d_p, was found to be (261±2.5) nm. The sphere shows the approximate size of a chromaffin granule (350 nm) for comparison. *Inset* The rapid decay of fluorescence as a is further increased shows the dramatic optical sectioning achieved upon evanescent excitation. For larger distances into the aqueous solution, a second, linear component of excitation light became dominant. Whereas the evanescent component rapidly decays away, the propagating light even slightly increases with distance along the optical axis. Linear extrapolation of the non-evanescent light contribution to $a=0$ yields an estimate for the proportion of non-evanescent fluorescence at the interface. The evanescent wave contributes more than 96.2% of the total excitation intensity at $a=0$

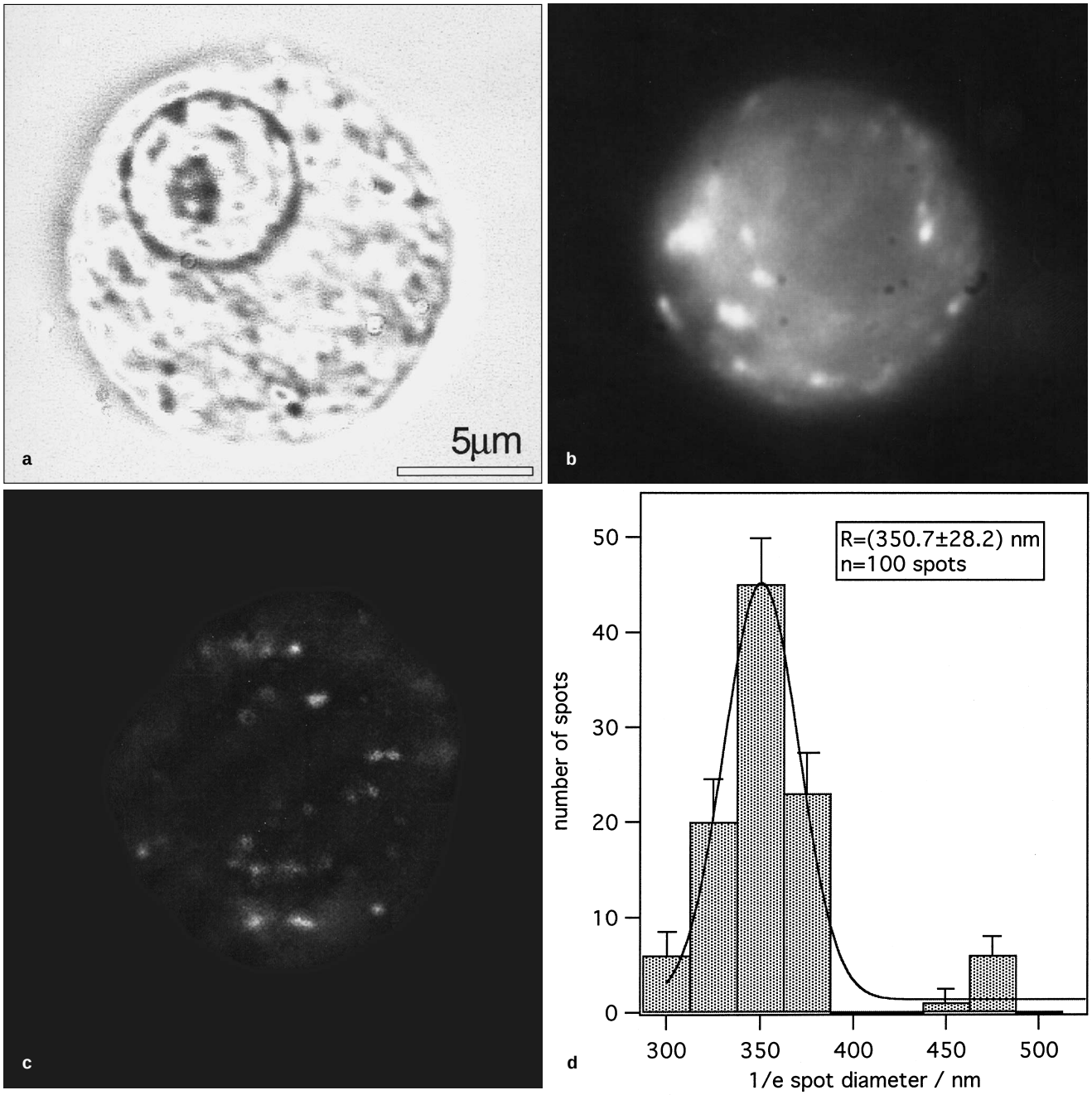

Fig. 3 Images under non-stimulated conditions **a** Trans-illumination and fluorescence images (**b, c**) of resting cells. Chromaffin granules were stained with 40 nM Lysotracker Green. The penetration depth was found to be (261 ± 2.5) nm by probing the evanescent field with fluorescent beads at different distances from the interface. Laser intensities were ≈ 0.65 mW post-fibre. The scalebar is 5 µm. Whereas the epi-image appears blurred and structureless, clear spots show up in the TIR image. Note the dramatically reduced out-of-focus signal in the case of evanescent wave excitation. **d** Distribution of $1/e^2$ spot radii in TIRF images of chromaffin cells. 100 Spots were taken from 3 cells stained with 40 nM *Lysotracker Green*. The average spot size was (350.7 ± 28.2) nm when fitted with a normal distribution. A second, less pronounced peak was centred around 480 nm (see text). **e** Fluctuation analysis by time-averaging 100 consecutive frames. The average image was subtracted from individual images. The remaining annular fluorescence pattern corresponds to a lateral agitation with an amplitude of (112 ± 34) nm. **f** Fluorescence intensity (FI) histogram of a TIRF image of a labeled chromaffin cell under non-stimulated conditions, corrected for the background signal. Data are plotted as occurrence vs. − ln (FI). Two peaks were clearly discernible from the weaker signal at the low-intensity end of the distribution. In resting cells, we found a ratio of peak heights, FI_{peak1}/FI_{peak2} of ~1.208. Substituting $\Delta z \pm dz = d_p \ln(FI_{peak1}/FI_{peak2}) \pm dz \approx 49.4 \pm 15$ nm, where $dz \approx 15$ nm is the accuracy of measuring z

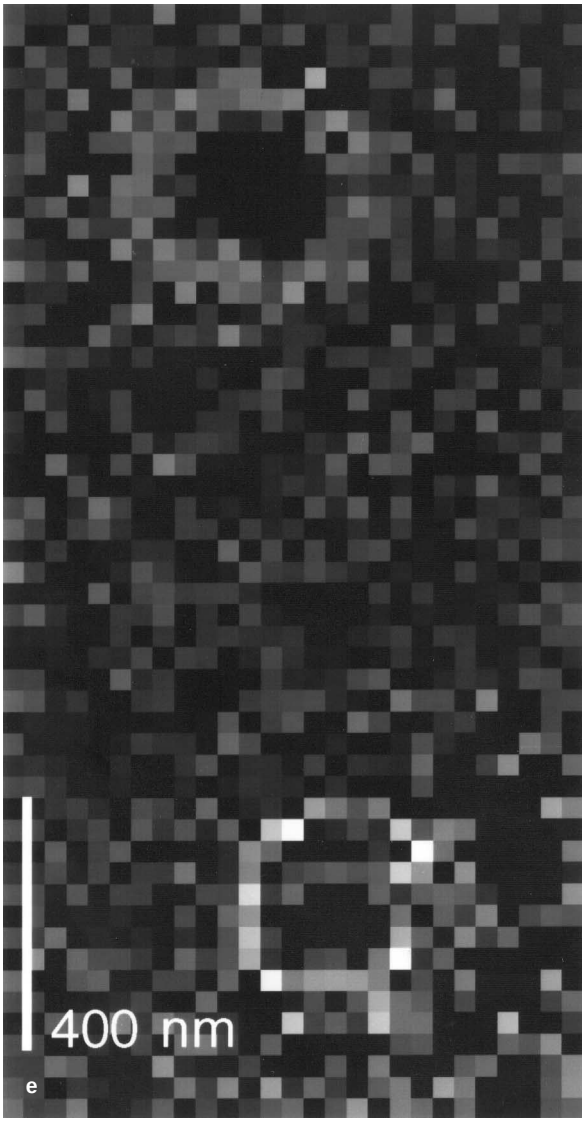

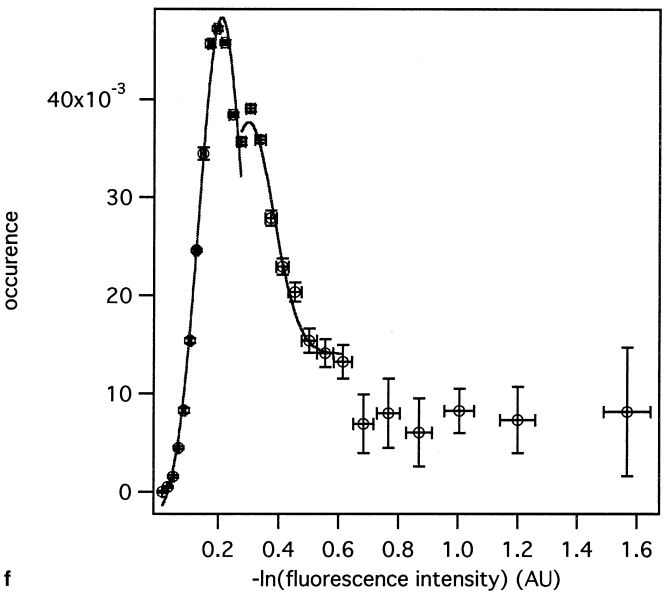

4.2.4 Agitation of fluorescent spots

Analysis of consecutive frames reported agitation of the fluorescent spots about their mean positions. Average displacements were of the order of a fraction of the spot diameter and occurred randomly in any direction. In the *z*-direction, this random movement was apparent as a 'twinkle' in the spot intensity as the vesicle bounces up and down in the evanescent field. From these fluorescence fluctuations we tried to infer the jitter along the optical axis by assuming that vesicles were moving up and down. With $d_p = (261 \pm 2.5)$ nm and $dz \approx 15$ nm known from our previous calibration measurements, we measured excess noise of $\approx 5\%$, corresponding to (28.4 ± 15) nm. We determined the lateral mobility by time-averaging 100 consecutive frames, recorded at 10 Hz. The average image was subtracted from individual images. This approach allows one to study positional fluctuations beyond the resolution limit and is in close analogy to stationary noise analysis (Neher and Stevens 1977; Sigworth 1980; DeFelice 1981). The remaining averaged images showed an annular fluorescence pattern corresponding to a lateral movement with an amplitude of (112 ± 34) nm (Fig. 3 e). Assuming free diffusion in 2 dimensions, the equivalent diffusion coefficient is 0.7×10^{-11} $cm^2 s^{-1}$.

4.2.5 Fluorescence intensity histograms

Fluorescence intensity (FI) histograms of the pixels in images of resting cells consistently displayed two peaks (Fig. 3 f) that could be fitted by Gaussian distributions, $f(FI) = K_0 + K_1 \exp(-((FI - K_2)/K_3)^2)$. The variance, K_3, was equal within 2% for all images and within $<5\%$ for images between any two cells, consistent with the presence of a fairly uniform size distribution of fluorescently labeled vesicles. The presence of two peaks gives rise to a variety of interpretations which will be addressed in the Discussion.

4.2.6 Depletion of the visible pool within hundreds of milliseconds after depolarisation

We studied the coupling of destaining to the stimulus triggering secretion. Depolarizing the plasma membrane by local puff application of high potassium extracellular solution, we increased $[Ca^{2+}]_i$ by evoking Ca^{2+}-influx through voltage-activated Ca^{2+}-channels. After stimulation, single spots vanished in an all-or-none fashion. After one minute of application of high external potassium solution the 'visible pool' was almost entirely depleted (Fig. 4 c).

Upon perfusion with standard external solution the area density of spots recovered to its initial value within (6 ± 1.3) minutes (Fig. 4 d). Destaining was blocked in experiments where Ca^{2+} was replaced with Mg^{2+} in the extracellular solution. Destaining was restored in high Ca^{2+}-solution (data not shown).

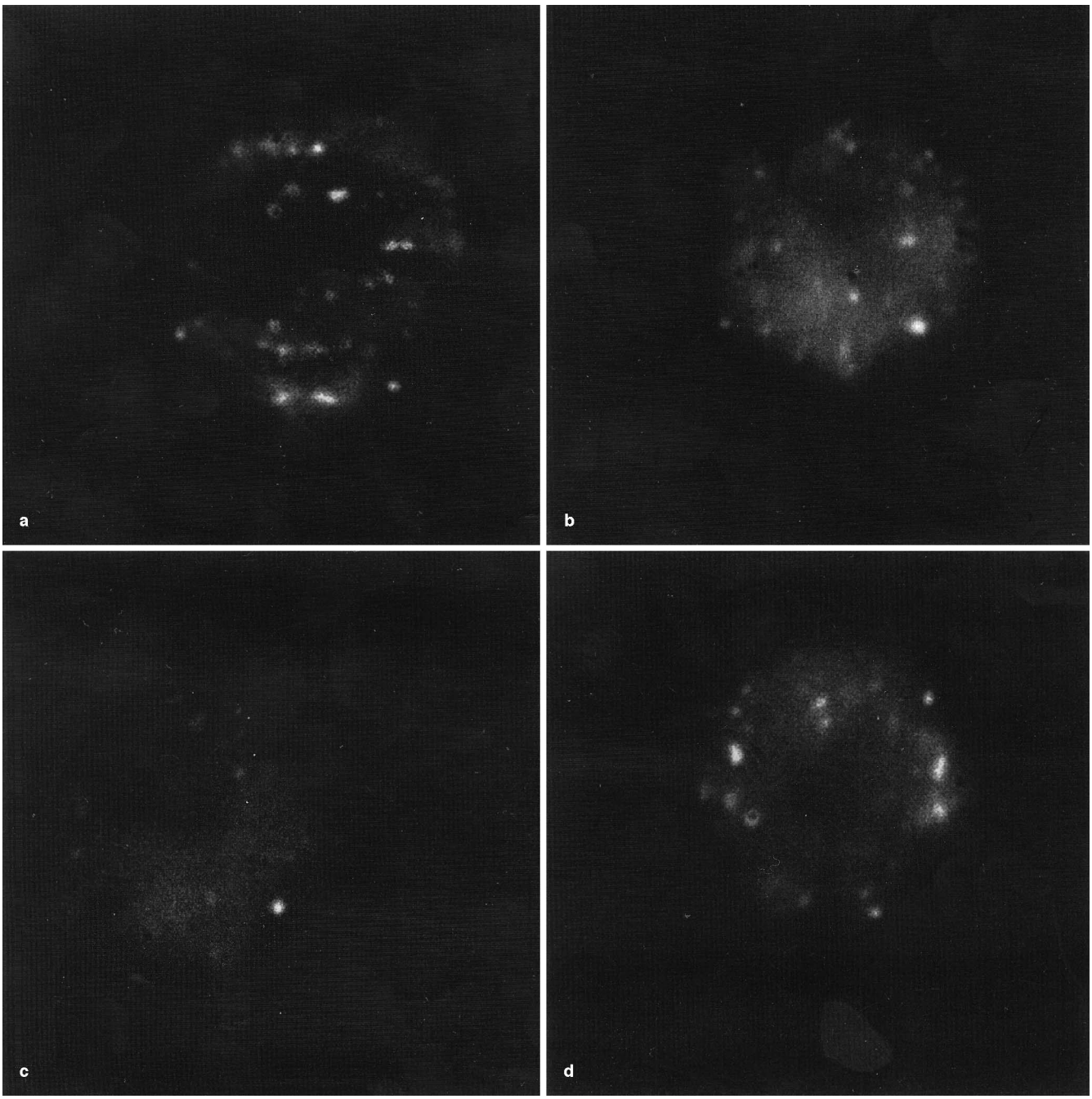

Fig. 4 TIRFM visualizes exocytosis of secretory granules. TIRF images of a chromaffin cell stained with 40 nM *Lysotracker* Green. Fluorescence excitation at 488 nm, 0.65 mW at an angle $\theta = 66.5°$. Images are taken with the Zeiss 100×1.0w lens with an additional 2× tube lens. Integration times were 60 ms. 100 ms (**a**) and 1 s (**b**) after local puff application of high potassium and (**c**) after 5 min wash with standard external solution. Bright spots were clearly resolvable and decreased upon stimulation. The 'visible pool' of vesicles was depleted within (1±0.2) s ($n = 33$). Full recovery was observed after (6±2) min (**d**)

4.2.7 Characteristic temporal changes in FI histograms

FI histograms changed reproducibly during application of high potassium extracellular solution and wash; whereas the total fluorescence intensity started to decrease within 100 ms after stimulation, the first peak slightly shifted to brighter intensities while the number of very bright pixels even slightly decreased. The second peak remained fairly constant before merging with the first peak after ≈300 ms. By 1 s after the onset of the stimulus, we observed an almost total loss of fluorescence (Fig. 5, fifth trace) ($n = 23$). An almost complete restoration of the initial FI distribution was observed after (6±1.3) min ($n = 34$) after wash with low-potassium extracellular solution (Fig. 5, last trace).

4.2.8 TIRFM reports the fusion of secretory vesicles

Acidotropic fluorescent dye molecules accumulate in the vesicle lumen and should be released along with transmit-

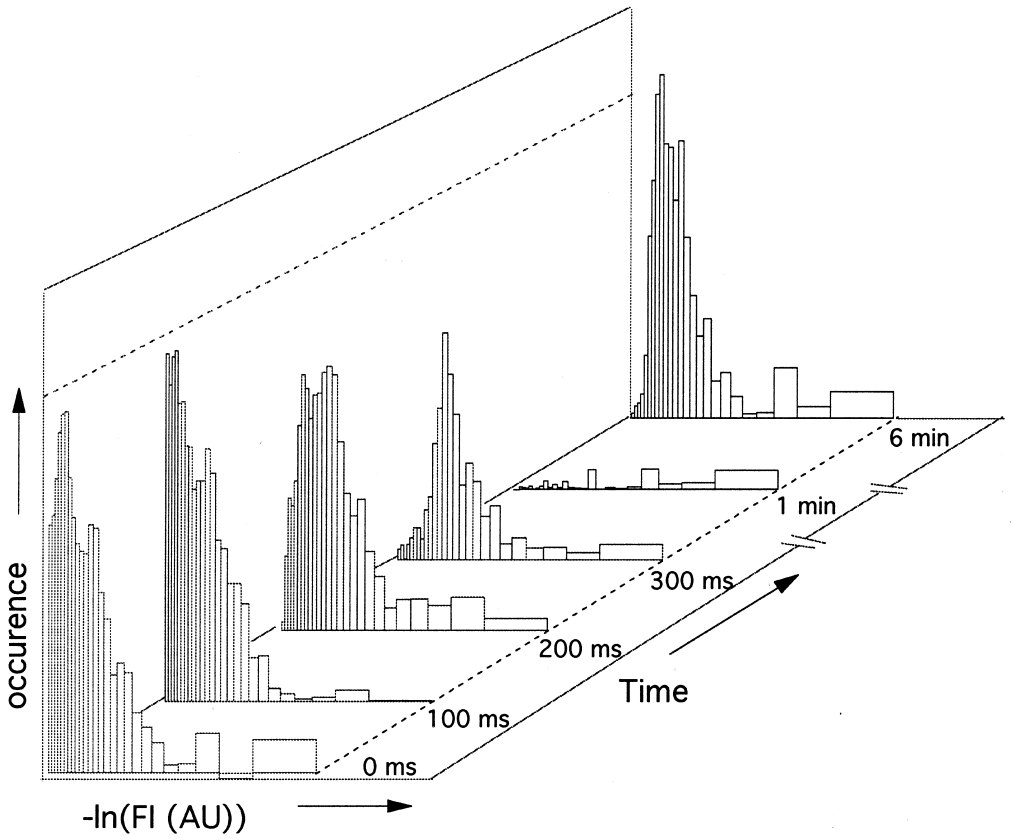

Fig. 5 Temporal changes of FI histograms with time. FI histograms changed reproducibly during application of high potassium extracellular solution and wash; total FI started to decrease within 100 ms after stimulation, whilst the first peak slightly shifted to brighter intensities. The number of very bright pixels even slightly decreased. The second peak remained fairly constant before merging with the first peak after ≈300 ms. By 1 s after the onset of the stimulus, we observed an almost total loss of fluorescence (Fig. 6, fourth trace) ($n=23$). An almost complete restoration of the initial FI distribution was observed (6 ± 1.3) min ($n=34$) after wash with low-potassium extracellular solution (last trace). The slight (≤1.5%) shift of the distribution in the direction of lower intensities might be attributed to photobleaching

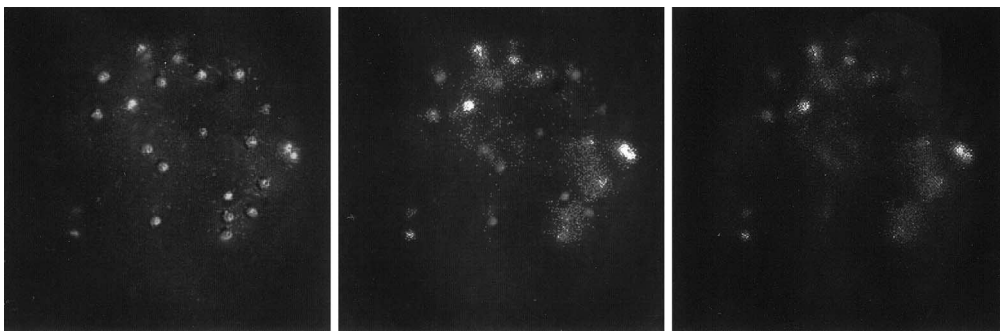

Fig. 6 Release of dye molecules and destaining. Fusion of secretory granules is detected by release of dye molecules into the extracellular fluid. This process was tightly coupled to depolarization-triggered Ca^{2+}-influx. Fast CCD imaging traces the brief appearance of a 'cloud' that quickly dilutes into the extracellular space. Integration times were 60 ms

ter upon fusion of the vesicle. Indeed, local destaining was accompanied by the brief (one to three 60-ms frames) appearance of a fluorescent 'cloud' that quickly dissipated, (Fig. 6). Diminished fluorescence intensity could also arise from the movement of vesicles away from the plasma membrane or the photobleaching of vesicles excited by the evanescent field. The former event, which was recognized by the disappearance of a spot without the appearance of a fluorescent cloud, was relatively rare (≤3% of events). Photobleaching was negligible in our conditions as indicated by the slight shift in the FI histograms (Fig. 5), with the fluorescences intensity of single spots diminishing approximately $1.3\pm0.2\%$ ($n=5$) over 6 minutes. TIRFM easily allows one to acquire time series with more than 500 exposures.

5 Discussion

We have monitored the behaviour of single secretory vesicles in bovine adrenal chromaffin cells using total internal reflection fluorescence microscopy (TIRFM). A laser beam was aimed at supercritical angle at the bottom of a coverslip on which cells were grown. The elicited evanescent wave selectively excited fluorescently labeled vesicles located in a thin optical slice near the coverslip.

Switching from epifluorescence excitation to TIR illumination resulted in the emergence of discrete bright spots out of a more diffuse fluorescent haze. The number of vesicles per unit area, $(1.07 \pm 0.11)\ \mu m^{-2}$ was stable in unstimulated cells; however, potassium stimulation resulted in spots disappearing. Continuous bath application of K^+ or repeated stimulation resulted in an almost complete loss of fluorescence within (1 ± 0.2) s ($n = 34$). Recovery was observed after (6 ± 1.3) min.

5.1 Depth of penetration of the evanescent field

The penetration depth of the evanescent field was determined by placing fluorescent beads at different known distances from the interface layer. For an angle of incidence of 66.5°, the excitation intensity decayed exponentially with a space constant of (261 ± 2.5) nm. This is in very good agreement with the theoretical value of 265.91 nm calculated according to Eq. (2). At $a = 2d_p$, less than 5% ($1/e^2$) of the excitation light at $a = 0$ remained. In terms of vesicle diameters ($D = 2R \approx 350$ nm), at $a = D$, $2D$ or $3D$ this decay amounts to 26.1%, 6.8% and 1.78% of the signal at the interface, respectively. Thus TIRFM should allow the selective visualization of a monovesicular layer of vesicles near to or docked at the plasma membrane.

We have also performed experiments in which the distance between bead and interface was fixed while the angle of incidence was varied. $FI(\theta)$ closely followed Eq. (2). Moreover, it was possible, starting from the measured FI and a known angle of incidence to calculate the position and diameter of a 200-nm bead with a precision of ±10 nm (data not shown).

5.2 TIRFM allows one to study secretion at single vesicle resolution

5.2.1 Staining

Dye solutions of AO exhibit multicolour fluorescence most likely due to the formation of monomers, dimers and polymers (Zanker 1952; Steiner and Beers 1961). Using 5 µm AO, we observed green fluorescent spots in chromaffin cells. When we repeated experiments with Lysotracker dyes, we observed similar staining in chromaffin cells and reproduced the bimodal size and intensity distributions found with AO.

5.2.2 Calibration of the evanescent field in vivo

The in vitro measurements with fluorescent beads established that our equipment could indeed be used to elicit TIR and, furthermore, provided some estimates of the depth of penetration of the evanescent wave. When living cells are studied, however, the actual penetration depths may not be as estimated in the in vitro conditions. At the cell-coverslip contact region, an inhomogeneous multi-layer of optical phases distorts the evanescent field. Each phase has a distinct refractive index ($n_{lipid} \approx 1.41$, $n_{cytosol} \approx 1.33 - 1.36$, proteins up to $n \approx 1.58$) inducing light scattering and complicating the calculation of the true critical angle and d_p. Additional light scattering arises from cellular debris at the optical interface, dust particles and microbubbles in the glass and immersion oil. In addition, the cell does not make flat contact with the substrate (Axelrod 1981; Thompson et al. 1993; Olveczky et al. 1997). Negative staining experiments in which we applied dye to the extracellular solution indicated that the cell attaches to the substrate in a patchy manner (data not shown). Time-dependent changes, such as cell movement or swelling introduced by application of high K^+ or vigorous exocytosis further undermine the calibration. Fortunately, although calculation of the depth of evanescent wave penetration with cells is more complicated than with fluorescent beads, we have found empirically that TIRFM nevertheless allows one to locate vesicles in a thin optical section at the base of a cell (see below).

5.2.3 Spot size distribution

Bright spots of fairly uniform size were seen in images of resting cells, incubated with acidotropic dyes. Spot sizes were centred at about (350.7 ± 28.2) nm, in good agreement (326–365 nm) with EM data of large dense core vesicles (LDCVs) (Winkler and Westhead 1980; Parsons et al. 1995). Histograms of the spots' $1/e^2$ diameters revealed a second though less pronounced peak at about 480 nm. The larger spots might be attributed to stained lysosomes (Robbins and Marcus 1963; Robbins 1964) or other acidic membrane-delimited compartments such as trans-Golgi vesicles or endosomes. However, such spots were seen to undergo exocytosis, which would not be expected of non-vesicular organelles. An alternative explanation for the population of larger spots might be compound exocytosis, i. e. vesicles fusing to each other before fusing to the plasma membrane. Vesicle-vesicle fusion would give rise to a two-fold increase in volume. Under evanescent excitation with a space constant $d_p \approx 261$ nm, a spherical, dye-filled volume of $2 \cdot (4\pi/3 \cdot 350^3)\ nm^3$ would show up as a spot with 457 nm diameter (Eq. (4)), somewhat (0.95×) smaller than the observed ones. However, detracting from this hypothesis, we never observed spontaneous spot enlargement. Chromaffin cells have been shown to contain small clear synaptic-like vesicles (SCSVs) apart from LDCVs (Thomas-Reetz and De Camilli 1994). SCSVs are below the lateral resolution of our system but may well contribute to the dim diffuse background that was observed in TIRF images.

5.2.4 Vesicle fusion

The persistence of the fluorescent spots in the resting cells, and rapid disappearance of the spots upon application of stimuli of secretion would suggest that the spots are vesicles that undergo exocytosis. However, the most powerful

evidence that we were looking at exocytosis of secretory granules is that, when spots destained, we were sometimes able to visualize the extracellular release of dye molecules. We were not able to capture this rapid event in all cases, owing to the limited temporal resolution of our camera.

We did not observe incomplete destaining, i. e. release without full fusion. This does not necessarily contradict previous findings of transient or incomplete fusion (Neher 1993; Wightman et al. 1995, Albillos et al. 1997) since our optical system may not have had the sensitivity to observe such changes.

5.3 Possible interpretations of the bimodal distribution of fluorescence in FI histograms

FI histograms revealed a bimodal distribution of fluorescence within the visible pool of granules. Bright pixels vanished first, consistent with fusion of those vesicles closest to the plasma membrane and dye being released onto the interface. This first phase was followed by a fast re-supply of fluorescence from darker pixels, observed as a shift of the second peak to brighter intensities. Upon persisting stimulation, this second peak is also lost.

It is tempting to interpret the bimodal fluorescence distribution in terms of physiologically distinct states, e. g. a docked, immature state and docked, release-ready ("primed") state. Given the inhomogeneity of d_p due to local changes in refractive index, we prefer to refrain from speculating and list possible explanations instead. Generally, discrete fluorescence signals may reflect two populations of vesicles, but could also stem from two components of evanescent excitation, or discrete local dielectric properties, or a combination of these. Fluorescence intensity data are not sufficient to distinguish among the possibilities.

5.3.1 Different populations of vesicles?

One obvious interpretation would be that there are two populations of vesicles at different distances from the plasma membrane. From the ratio of peak fluorescence intensities FI_{peak1}/FI_{peak2} of ~1.208, it should be possible to calculate the difference in distances for these two populations. For simplicity we make the assumptions that the average $d_{p,cell}$ is well approximated by d_p determined in vitro, and that vesicles having the same radius R have identical fluorescence (identical dye concentration). Substituting $\Delta z \pm dz = d_p \ln(FI_{peak1}/FI_{peak2}) \pm dz$ yields 49.4 ± 15 nm, where $dz \approx 15$ nm is the accuracy of measuring z (see results).

Another possible interpretation is that are two discrete levels of dye concentration in the vesicles or two differing intravesicular environments "seen" by the dye molecules, leading to different spectral properties. Earlier electrophysiological work (Beckenridge and Almers 1987) suggested that significant differences in electrochemical gradients exist across the granule membrane. The major source of the electrochemical gradient is the proton gradient. However, pH-dependent changes in the fluorescence emission of AO and *Lysotracker* were found to be insufficient to account for the difference in *FI* (data not shown).

A recent study combining amperometric and ΔC_m measurements in mouse adrenal slices suggests that the fast secretory component in chromaffin cells mainly represents fusion of a single population of LDCVs, each contributing (1.3 ± 0.7) fF to ΔC_m (Moser and Neher 1997). This would strengthen the assumption of one population of vesicles and support the idea that the bimodal fluorescence distribution is due to two different functional pools of vesicles. However, Kasai et al. have recently presented evidence of two different types of vesicles with distinct kinetics in chromaffin and PC12 cells (Kasai et al. 1996; Ninomiya et al. 1997). Thus, the issue of distinct populations appears not to have been finally resolved.

5.3.2 Bimodal fluorescence excitation

The bimodal FI distribution could also arise if evanescent excitation is not uniform for all vesicles at the plasma membrane. Undulations of the plasma membrane facing the coverslip or locally different refractive indices could conceivably result in two components, d_{p1} and d_{p2}, of the evanescent penetration depth. It is also possible that a fraction of the docked vesicles exist in a "hemifused state" (Vogel et al. 1993; Chernomordik et al. 1995) in which the inner leaflet of the plasma membrane lipid bilayer is fused to the vesicle outer leaflet. Such a structure is likely to be associated with dramatic changes in the local dielectric environment and is expected to influence the evanescent wave.

5.4 Is the 'visible pool' identical to the pool of readily-releasable granules?

We have introduced the concept of the 'visible pool' of vesicles. This is an operational definition that is dependent upon the decay length $d_p(\theta)$. Under cell-culture conditions, the average number of docked vesicles in chromaffin cells in EM was found to be 834 ± 42 (Parsons et al. 1995), or $1.83 - 0.91$ vesicles/μm^2 for cells of $12 - 17$ μm diameter, respectively. Parsons et al. give a value of (1.4 ± 0.1) μm^{-2}, corrected for the number of granules near, but not bound to the plasma membrane. The corrected value leads to an estimate of about 600 docked vesicles – close to the total C_m increases seen with Ca-triggered exocytosis in the absence of ATP (i. e. vesicles that were already ATP-primed), assuming 10 fF/μm^2 membrane surface area.

We measured the number of chromaffin granules in the *visible* pool upon evanescent excitation with a penetration depth of 261 nm. The number of vesicles was found to be 54 ± 12 ($n = 34$ cells) in a region of cell-substrate contact with $8 - 12$ μm diameter. This corresponds to (0.47 ± 0.11) to (1.07 ± 0.24) vesicles/μm^2 or 300 to 680 vesicles for a

chromaffin cell of 16 μm diameter, somewhat below the value of docked vesicles derived from EM. This discrepancy might be due to there being fewer vesicles at the plasma membrane attached to the coverslip, than over the rest of the cell. More importantly, the bottom of the cell is not flatly adherent to the coverslip. Therefore, evanescent excitation may only reach a variable portion of the total number of vesicles, presumably underestimating the number of docked granules. Finally, not all granules might have been stained.

Using a variant of TIRFM based upon total reflection of a laser beam directed through the periphery of a high-numerical aperture objective (Stout and Axelrod, 1989), Steyer and Almers (1996) reported a number of (1.47 ± 0.2) vesicles/μm^2. This 'prismless' geometry restricts beam incidence to a fixed angle, and was reported to result in a higher background of scattered light, possibly due to the use of peripheral rays (i. e. the outer region of the optical path) where lens aberrations are more likely to be of relevance (Axelrod, 1992). Steyer and Almers (1997) found 51 ± 0.6% of the points remaining after stimulation in 6 min in 60 mM K and 5 mM Ca. This might indicate that a larger population of vesicles is visualized, probably owing to a larger penetration depth compared to the variable-angle approach. In either case the visible pool only partly coincides with the pool of release-ready granules defined electrophysiologically.

5.5 Mobility of single granules

We found in resting cells that the number and distribution of visualized vesicles was fairly stable. Only occasionally, vesicles were seen to migrate into the visible pool. Their approach seemed as if they were transported unidirectionally almost perpendicular to the plasma membrane. Upon arriving at the membrane, vesicles showed little lateral mobility. Average displacements in the $x-y$ plane were of the order of a fraction of the spot diameter and occurred in random direction with an amplitude of (112 ± 34) nm. Fluctuations in FI corresponded to vesicles moving (28 ± 15) nm along the z-axis. On stimulation, vesicles fused where they had previously docked at the membrane, and often in clusters.

Our results suggest highly organized sub-plasmalemmal structures, directing or transporting vesicles to their would-be docking sites and keeping them in position. Docking is accompanied by a dramatic decrease in the mobility in the z direction, a characteristic that helps distinguish already-docked vesicles from vesicles still approaching their docking sites.

The axial and lateral mobility differ by almost an order of magnitude. This would be consistent with vesicles being tightly linked to a membrane-resident docking site. The bond would restrict its lateral and axial mobility, whereas the binding site itself is slowly diffusing with the vesicle attached to it with a free (2-D) diffusion coefficient of 0.7×10^{-11} $cm^2\,s^{-1}$. This is of the order of magnitude of other large membrane-resident proteins.

5.6 Comparison of TIRFM with other techniques

We have shown that TIRFM can be used to observe single secretory vesicles docking, residing at the plasma membrane and undergoing exocytosis. While its spatial resolution is less than that of an electron microscope, TIRFM offers the advantage of enabling studies in *living* cells. In comparison with standard confocal imaging, TIRFM has the advantage of confining excitation to a thin optical slice near the cell-substrate interface. This highly efficient use of illuminating photons reduces photodamage and permits image acquisition at videorate, since complicated scanning and image reconstruction techniques are not required.

Membrane capacitance measurements (Neher and Marty 1982), see Henkel and Almers (1996); Matthews (1996) for recent reviews, and amperometric detection (Wightman et al. 1991) have enabled studies of single vesicle fusion and transmitter release at millisecond time resolution. With these approaches, it has also been possible to infer what happens in steps preceding vesicle fusion; however, complex kinetic modeling was required (Heinemann et al. 1994; Neher and Zucker 1993; Thomas et al. 1993). TIRFM, in contrast, does not offer quite the same high time resolution, but it has the advantage of permitting direct observation of secretory granules in the stages prior to fusion and it provides detailed spatial resolution.

Thus, TIRFM is complementary to other assays of secretion, offering selective advantages for some purposes. Future studies will relate the visible vesicle pool to the functional states of secretory vesicles, perhaps shedding light on the roles of specific roles of regulatory proteins.

Acknowledgements We would like to thank F. Friedlein and M. Pilot for the cell preparation, S. Voigt and W. Lessner for expert technical support, Drs. A. Brüggemann and M. Hunter for critical feedback on the manuscript and Profs. E. Neher, F. Lanni and W. W. Webb for helpful discussion and suggestions. This work was supported by a British Council Academic Research Collaboration (ARC) grant to RHC and WS.

References

Albillos A, Dernick G, Horstmann H, Almers W, Alvarez de Toledo G, Lindau M (1997) The exocytotic event in chromaffin cells revealed by patch amperometry. Nature 389: 509–512

Agard DA, Hiraoka Y, Shaw P, Sedat JW (1989) Fluorescence microscopy in three dimensions. Methods Cell Biol 30 (Part B): 353–377

Axelrod D (1981) Cell-substrate contacts illuminated by TIRF. J Cell Biol 89: 141–145

Axelrod D, Hellen EH, Fulbright RM (1992) Total internal reflection fluorescence. In: Lakovicz JR, Topics in fluorescence spectroscopy. Plenum Press, New York, p 289

Beckenridge LJ, Almers W (1987) Currents through the fusion pore that forms during exocytosis of a secretory vesicle. Nature 328: 814–817

Burghardt TP, Thompson NL (1984) Evanescent intensity of a focused gaussian light beam undergoing total internal reflection in a prism. Opt Eng 23: 62–67

Chad JE, Eckert R (1984) Calcium domains associated with individual channels can account for anomalous voltage relations of Ca-dependent responses. Biophys J 45: 993–999

Cheek TR, O'Sullivan AJ, Moreton RB, Berridge MJ, Burgoyne RD (1989) Spatial localization of the stimulus-induced rise in cytosolic Ca^{2+} in bovine adrenal chromaffin cells. FEBS Lett 247: 429–434

Chernomordik L, Chanturiya A, Green J, Zimmerberg J (1995) The hemifusion intermediate and its conversion to complete fusion: regulation by membrane composition. Biophys J 69: 922–929

Chow RH, Klingauf J (1994) Time course of Ca^{2+} concentration triggering exocytosis in neuroendocrine cells. Proc Natl Acad Sci USA 9: 12 765–12 769

Cleeman L, Morad M (1997) Visualization of calcium sparks in heart cells with total internal reflection fluorescence microscopy (TIRF). Biophys J 72: A45

De Felice LJ (1981) Introduction to membrane noise. Plenum Press, New York

Denk W, Strickler JH, Webb WW (1990) Two-photon laser scanning fluorescence microscopy. Science 248: 73–76

Denk W, Yuste R, Svoboda K, Tank DW (1996) Imaging calcium dynamics in dendritic spines. Curr Op Neurobiol 6: 372–378

Etter EF, Kuhn MA, Fay FS (1994) Detection of changes in near-membrane Ca^{2+} concentration using a novel membrane-associated Ca^{2+} indicator. J Biol Chem 269: 10 141–10 149

Fox GQ (1996) A morphometric analysis of exocytosis in KCl-stimulated bovine chromaffin cells. Cell Tissue Res 284: 303–316

Funatsu T, Harada Y, Tokunaga M, Saito K, Yanagida T (1995) Imaging of single fluorescent molecules and individual ATP turnovers by single myosin molecules in aqueous solution. Nature 374: 555–559

Gingell D, Todd I, Bailey J (1985) Topography of cell-glass apposition revealed by total internal reflection fluorescence of volume markers. J Cell Biol 100: 1334–1338

Goos F, Hänchen H (1947) Ein neuer und fundamentaler Versuch zur Totalreflexion. Ann d Physik 6: 333–346

Ha T, Enderle T, Ogletree DF, Chemla DS, Selvin PR, Weiss S (1996) Probing the interaction between 2 single molecules – fluorescence resonance energy-transfer between a single-donor and a single acceptor. Proceedings of the National Academy of Sciences of the United States of America 93: 6264–6268

Harrick NJ (1965) Electric field strengths at totally reflecting interfaces. J Opt Soc Am 55: 851

Harrick NJ (1967) Internal reflection spectroscopy. Wiley, New York London Sydney

Heinemann C, Rüden L von, Chow RH, Neher E (1993) A two-step model of secretion control in neuroendocrine cells. Pflügers Arch 424: 105–112

Henkel AW, Almers W (1996) Fast steps in exocytosis and endocytosis studied by capacitance measurements in endocrine. Cells Curr Op Neurobiol 6: 350–357

Hiraoka Y, Sedat JW, Argard DA (1990) Determination of the three-dimensional imaging properties of a light microscope system – partial confocal behaviour in epifluorescence microscopy. Biophys J 57: 325–333

Huang Z, Pearce KH, Thompson NL (1994) Translational diffusion of bovine prothrombin fragment 1 weakly bound to supported planar membranes: measurement by total internal reflection with fluorescence pattern photobleaching recovery. Biophys J 67: 1754–1766

Jankowski JA, Schroeder TJ, Ciolkowski EL, Wightman RM (1993) Temporal characteristics of quantal secretion of catecholamines from adrenal medullary cells

Kasai H, Takagi H, Ninomiya Y, Kishimoto T, Ito K, Yoshida A, Yoshioka T, Miyashita Y (1996) Two components of exocytosis and endocytosis in phaeochromocytoma cells studied using caged Ca^{2+} compounds. J Physiol 494: 53–65

Klingauf J, Neher E (1997) Modelling buffered Ca^{2+} diffusion near the membrane: implications for secretion in neuroendocrine cells. Biophys J 72: 674–690

Lanni F, Waggoner AS, Taylor DL (1985) Structural organization of interphase 3T3 fibroblasts studied by TIRFM. J Cell Biol 100: 1091–1102

Lassen B, Malmsten M (1996) Competitive protein adsorption studied with TIRF and ellipsometry. J Coll Interface Sci 179: 470–477

Lipp P, Niggli E (1993) Ratiometric confocal Ca^{2+}-measurements with visible wavelength indicators in isolated cardiac myocytes. Cell Calcium 14: 359–372

Llinas R, Sugimori M, Silver RB (1992) Microdomains of high calcium concentration in a presynaptic terminal. Science 256: 677–679

Macklin JJ, Trautman JK, Harris TD, Brus LE (1996) Imaging and time-resolved spectroscopy of single molecules at an interface. Science 272: 255–258

Marom E, Chen B, Ramer OG (1979) Spot size of focused truncated gaussian beams. Opt Eng 18: 79–81

Matthews G (1996) Synaptic exocytosis and endocytosis: capacitance measurements. Curr Op Neurobiol 6: 358–364

Monck JR, Fernandez JM (1996) The fusion pore and mechanisms of biological membrane fusion. Curr Opp Cell Biol 8: 524–533

Monck JR, Robinson IM, Escobar AL, Vergara JL, Fernandez JM (1994) Pulsed laser imaging of rapid Ca^{2+} gradients in excitable cells. Biophys J 67: 505–514

Moser T, Neher E (1997) Estimation of mean exocytic vesicle capacitance in mouse adrenal chromaffin cells. Proc Natl Acad Sci USA 94: 6735–6740

Neher E, Stevens CF (1977) Conductance fluctuations and ionic pores in membranes. Annu Rev Biophys Bioeng 6: 345–351

Neher E (1986) Concentration profiles of intracellular calcium in the presence of a diffusable chelator. Exp Brain Res 14: 80–96

Neher E, Marty A (1982) Discrete changes of cell membrane capacitance observed under conditions of enhanced secretion in bovine adrenal chromaffin cells. Proc Natl Acad Sci USA 79: 6712–6716

Nehr E (1993) Secretion without full fusion. Nature 363: 497–498

Neher E, Zucker R (1993) Multiple calcium-dependent processes related to secretion in bovine chromaffin cells. Neuron 10: 21–30

Ninomiya Y, Kishimoto T, Yamazawa T, Ikeda H, Miyashita Y, Kasai H (1997) Kinetic diversity in the fusion of exocytotic vesicles. EMBO J 16: 242–251

Oheim M, Chow RH, Stühmer S (1997) Total internal reflection fluorescence microscopy (TIRFM) resolves vesicle dynamics between distinct submembranous pools prior to fusion. Biophys J 72: A215

Olveczky BP, Periasamy N, Verkman AS (1997) Mapping fluorphore distributions in 3 dimensions by quantitative multi-angle total internal reflection fluorescence microscopy (MA-TIRFM). Biophys J 72: A212

Parsons TD, Coorssen JR, Horstmann H, Almers W (1995) Docked granules, the exocytic burst, and the need for ATP hydrolysis in endocrine cells. Neuron 15: 1085–1096

Pawley JB (1995) Handbook of biological confocal microscopy. Plenum Press, New York London

Piston DW, Kirby MS, Cheng H, Lederer WJ, Webb WW (1994) Two-photon-excitation fluorescence imaging of tree-dimensional calcium-ion activity. Appl Opt 33: 662–669

Robbins E, Marcus PI (1963) Dynamics of acridine orange-cell interaction. J Cell Biol 18: 237–250

Robbins E, Marcus PI, Gonatas NK, Micali A (1964) II. Dynamics of acridine orange-cell interaction. J Cell Biol 21: 49–62

Robinson IM, Finnegan JM, Monck JR, Wightman RM, Fernandez JM (1995) Colocalization of calcium entry and exocytotic release sites in adrenal chromaffin cells. Proc Natl Acad Sci USA 92: 2474–2478

Robinson IM Yamada M, Carrion-Vasquez M, Lennon VA, Fernandez JM (1996) Specialized release zones in chromaffin cells examined with pulsed laser imaging. Cell Calcium 20: 181–201

Sigworth FJ (1980) The variance of sodium current fluctuations a the node of ranvier. J Physiol 307: 97–129

Smith SJ, Buchanan J, Osses LR, Charlton MP, Augustine GJ (1993) The spatial-distribution of calcium signals in squid presynaptic terminals. J Physiol 472: 573–593

Steiner RF, Beers RFJ (1961) Polynucleotides. Elsevier, Amsterdam

Steyer JA, Almers W (1996) Single chromaffin granules beneath the plasma-membrane viewed by TIR fluorescence microscopy. Biophys J 70: A308

Steyer JA, Horstmann H, Almers W (1997) Transport, docking and exocytosis of single secretory granules in live chromaffin cells. Nature 388: 474–478

Stout AL, Axelrod D (1989) Evanescent field excitation of fluorescence by epi-illumination microscopy. Appl Opt 28: 5237 – 5242
Südhof TC (1995) The synaptic vesicle cycle: a cascade of protein-protein interactions. Nature 375: 645 – 653
Südhof TC, Rizo J (1996) Synaptotagmins: C2-domain proteins that regulate membrane traffic. Neuron 17: 379 – 388
Svoboda K, Denk W, Knox WH, Tsuda S (1996) 2-photon-excitation scanning microscopy of living neurons with a saturable bragg reflector mode-locked diode-pumped Cr-LiSrAlFl laser. Opt Lett 21: 1411 – 1413
Thomas P, Wong JG, Almers W (1993) Millisecond studies of secretion in single rat pituitary cells stimulated by flash photolysis of caged calcium. EMBO J 12: 303 – 306
Thomas-Reetz A, DeCamilli P (1994) A role for synaptic vesicles in non-neuronal cells: clues from pancreatic beta cells and from chromaffin cells. FASEB J 8: 209 – 216
Thompson NL, Pearce KH, Hsieh HV (1993) Total internal reflection fluorescence microscopy: application to substrate-supported planar membranes. Eur Biophys J 22: 367 – 378
Vogel SS, Leikina EA, Chernomordik LV (1993) Lysophospatidylcholine reversibly arrests exocytosis and viral fusion at a stage between triggering and membrane merger. J Biol Chem 268: 25 764 – 25 768
Wightman RM, Jankowski JA, Kennedy RT, Kawagoe KT, Schroeder TJ, Leszczszyn FJ, Near JA, Diliberto EJ, Viveros OH (1991) Temporarily resolved catecholamine spikes correspond to single vesicle release from individual chromaffin granules. Proc Natl Acad Sci USA 88: 10 754 – 10 775
Wightman RM, Schroeder TJ, Finnegan JM, Ciolkowski EL, Pihel K (1995) Time-course of release of catecholamines from individual vesicles during secretion at adrenal medullary cells. Biophys J 68: 383 – 390
Winkler H, Westhead E (1980) The molecular organization of adrenal chromaffin granules. Neuroscience 5: 1803 – 1823
Zanker V (1952) Z Phys Chem 199: 225 – 258